

# Meta-grating outcouplers for optimized beam shaping in the visible

CHAD ROPP,<sup>1,2\*</sup> ALEXANDER YULAEV,<sup>1,2</sup> DARON WESTLY,<sup>1</sup> GREGORY SIMELGOR,<sup>1</sup> AND VLADIMIR AKSYUK<sup>1</sup>

<sup>1</sup>Physical Measurement Laboratory, National Institute of Standards and Technology, Gaithersburg, Maryland 20899, USA

<sup>2</sup>Department of Chemistry and Biochemistry, University of Maryland, College Park, MD 20742, USA

\*chad.ropp@nist.gov

**Abstract:** Accurate coupling between optical modes at the interface between photonic chips and free space is required for the development of many on-chip devices. This control is critical in quantum technologies where large-diameter beams with designed mode profiles are required. Yet, these designs are often difficult to achieve at shorter wavelengths where fabrication limits the resolution of designed devices. In this work we demonstrate optimized outcoupling of free-space beams at 461 nm using a meta-grating approach that achieves a 16 dB improvement in the apodized outcoupling strength. We design and fabricate devices, demonstrating accurate reproduction of beams with widths greater than 100  $\mu\text{m}$ .

## 1. Introduction

Integrated photonics are enabling new technologies for compact sensing [1], metrology [2], and quantum computing [3]. Many applications require light to be sent off chip—for example to interrogate isolated atomic media [4–7]—which benefit from the miniaturization and manufacturability of integrated photonics. Such designs require mode couplers capable of generating free-space beams with different wavelengths, polarizations, and beam geometries. As examples, beams with large numerical apertures or large beam waists may be required for projecting optical [8] and magneto-optical traps (MOTs) [9,10], respectively. Accurate beam control can be realized using on-chip outcouplers combined with planar metasurfaces to modify the beam phase profile and polarization state [11]. Such platforms enable the integration of beams of multiple colors, profiles, and polarizations for unparalleled control of optical fields within a compact three-dimensional space.

Proper design of photonic outcouplers is important for generating pristine free-space beams. Grating couplers, which operate based on Bragg scattering [12], are often needed when light is coupled into or out from the device surface. To optimally match modes at the interface, grating couplers may be apodized and subwavelength meta-grating (MG) elements incorporated to provide continuous control of the outcoupling strength [13]. While subwavelength MGs have found many applications at telecom wavelengths [14–17], their use in the visible is more restricted by the resolution of lithography and process variations [18]. In addition, material losses become a major concern at visible wavelengths, requiring the consideration of trade-offs between loss performance and fabricability [19].

In this work we utilize an apodized design of subwavelength MGs using a silicon nitride platform to create large mode diameter outcouplers at 461 nm. This wavelength is used for laser cooling strontium atoms in MOTs and atomic clocks [20,21]. By strictly accommodating the limits of electron-beam lithography in our MG design we fabricate outcouplers that accurately reproduce elliptical collimated Gaussian beams with waists larger than 100  $\mu\text{m}$ . These beam profiles are strictly only achievable using a MG approach. Restricted by a minimum physical feature size of 30 nm, our MG design incorporates lines with effective widths down to 4.5 nm, providing a 16 dB improvement in the dynamic range of the outcoupling strength and smoother turn on of the beam profile compared to solid-line gratings. By establishing an equivalency between our MG and an effective solid-line design, we demonstrate an intuitive approach for

calculating the required apodization using two-dimensional modeling. Our MG performance at 461 nm relies critically on the use of sub-diffractive elements, whose designed anisotropy could be exploited in future designs to enable added functionality and polarization control [22].

## 2. Meta-grating design and performance

The photonic outcoupler is based on a two-stage extreme mode converter that enables beam shaping along two independent axes [23], shown in Fig. 1(a). The first stage is an evanescent coupler (EVC) that converts a single waveguide mode into a collimated slab-mode beam. The EVC operates based on evanescent coupling, which is controlled by spatially varying the gap between the waveguide and the dielectric slab along the direction of propagation (see Fig. S1 in the Supplement 1). The second stage is the MG outcoupler that converts the slab-mode beam into a free space beam (side view in Fig. 1(b)). Beam shaping is achieved in both stages by spatially varying the coupling strength between successive optical modes according to:

$$\Gamma(x) = \frac{B(x)}{1 - \int_{-\infty}^x B(x') dx'} \quad (1)$$

where  $x$  is the propagation direction and  $\Gamma(x)$  is the spatially varying coupling strength required to achieve the beam power profile  $B(x)$ , with unity total power [24]. Fig. 1(c-d) shows a Gaussian beam intensity profile with a  $1/e^2$  radius  $w_0 = 100 \mu\text{m}$ , and its corresponding  $\Gamma$ . This Gaussian profile has been truncated at  $1.5w_0$  for realization within a finite-sized device.

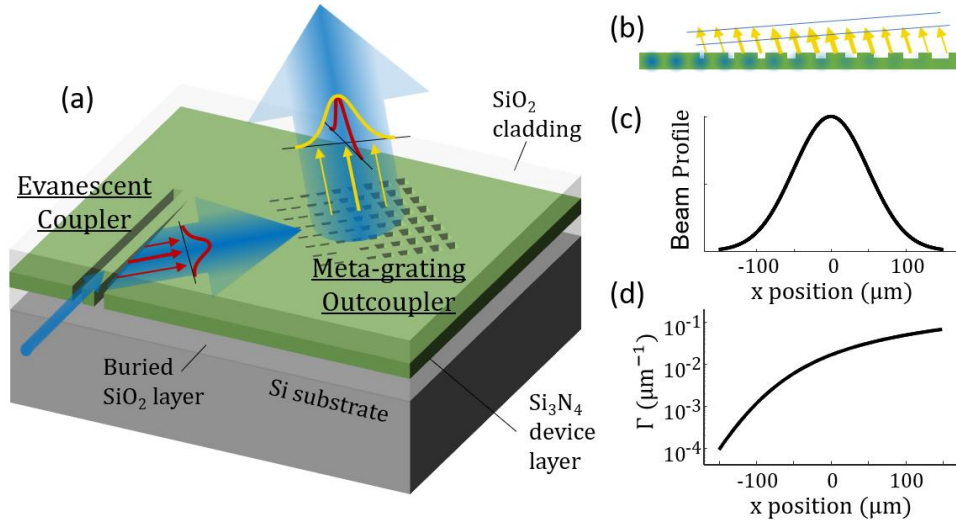


Fig. 1. Meta-grating outcoupler design (a) Extreme mode converter based on a two-stage design. The first stage is an EVC and the second is the MG outcoupler. Together the free-space beam can be shaped along two orthogonal directions (denoted red and yellow from each stage). (b) Side diagram of the apodized grating outcoupler, which shapes the beam profile and scatters collimated light into free space (yellow arrows). (c) An example Gaussian beam profile with a  $100 \mu\text{m}$  beam waist. (d) Spatial variation of outcoupling strength required to generate the beam profile in panel c.

The example profile requires varying  $\Gamma$  over nearly three orders of magnitude, which can be difficult to achieve given fabrication limitations—specifically for the grating outcoupler if it is composed of a solid-line grating. We calculate  $\Gamma$  for both the EVC and the grating outcoupler as a function of design parameters using finite element method simulation. Our simulated device consists of a  $150 \text{ nm}$  thick silicon nitride ( $\text{Si}_3\text{N}_4$ ) layer embedded in silicon dioxide ( $\text{SiO}_2$ ). For the EVC, we consider a uniform waveguide that is  $100 \text{ nm}$  wide and  $150$

nm thick and that couples in plane with a dielectric slab of the same thickness. With this geometry, the required range of  $\Gamma$  is achieved by varying the gap between the waveguide and the dielectric slab.  $\Gamma$  can be made arbitrarily weak by increasing the gap, while the strongest  $\Gamma$  requires a minimum gap of  $\approx 200$  nm, which is readily realizable using conventional lithography. In contrast, the grating outcoupler is more dependent on the minimum feature size. If we consider a single etch step design for the grating, then both the minimum and maximum  $\Gamma$  must be realized using the same etch depth. The strongest  $\Gamma$  is achieved at etch depths deeper than around 30 nm. If we chose this as our minimum depth, then the weakest  $\Gamma$  requires solid grating lines narrower than 5 nm, which is far below the resolution of electron-beam lithography based dry etch patterning.

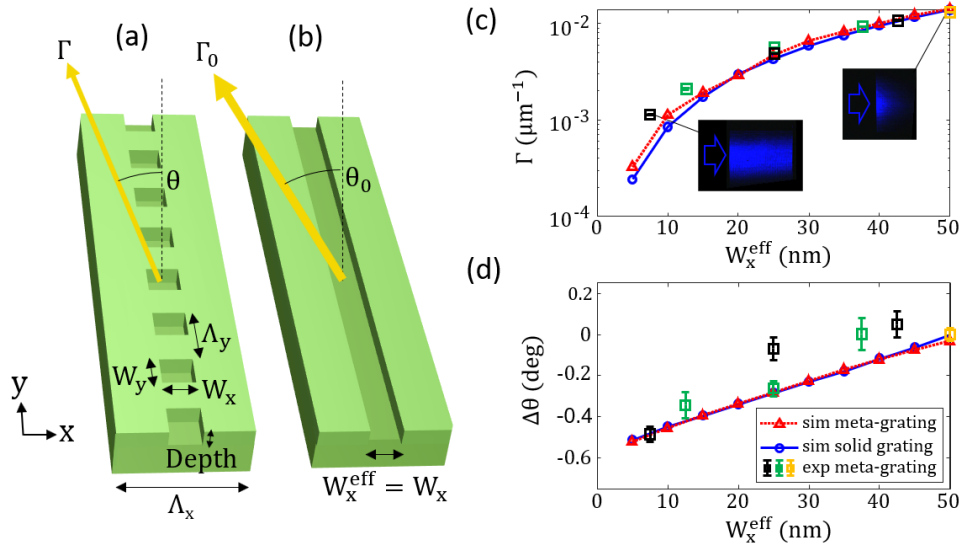


Fig. 2. Equivalence between meta- and solid-line gratings (a) A single MG line consisting of an array of subwavelength-sized etched elements. (b) A single line from a solid-line grating with the same width as the design in panel a. (c) The calculated outcoupling strength of the simulated MG (red), simulated solid-line grating (blue), and experimentally fabricated MGs as a function of  $W_x^{\text{eff}}$ . The experimental data includes designs with  $\Lambda_y = 200$  nm (black data),  $\Lambda_y = 120$  nm (green data), and with a solid grating design (orange data). Insets show optical images of the light scattered from several of the fabricated gratings, where the slab-mode light is incident from the left (denoted with a blue arrow). (d) The calculated change in outcoupling angle as a function of  $W_x^{\text{eff}}$  from the same data sets in panel c. In all experimental data, the error bars correspond to one standard deviation statistical uncertainty of the measurement.

To fabricate grating lines with weaker outcoupling strengths than can be realized with solid lines, we use the MG design shown in Fig. 2(a). The period of the MG,  $\Lambda_y$ , must be less than the wavelength of the slab mode to prevent in-plane scattering at normal incidence [13]. We consider a maximum  $\Lambda_y = 200$  nm, which is smaller than the wavelength of the fundamental TE slab mode, which propagates with a mode index of  $\approx 1.86$ . Considering that our minimal resolvable electron beam feature size is 30 nm, then the weakest MG line we can write has a filling fraction equal to that of a solid line with a width  $W_x^{\text{eff}} = 4.5$  nm, where we define

$$W_x^{\text{eff}} = \frac{W_x W_y}{\Lambda_y} \quad (2)$$

and  $W_x$  and  $W_y$  are the widths of the MG element (minimally 30 nm) along the x and y directions, respectively.

Figs. 2(c-d) show that MGs perform nearly identically to their filling-fraction equivalent solid-line gratings. We consider a uniform MG with  $W_x = 50$  nm, an etch depth of 37 nm, and

$\Lambda_x = 425$  nm—the period of the grating along the direction of propagation. We vary the filling fraction by changing  $W_y$  and calculate  $\Gamma$  and the change in emission angle,  $\Delta\theta = \theta - \theta_0$ , as a function of the calculated  $W_x^{\text{eff}}$  (red data) and compare it to a design with the MG replaced by a solid line grating with line width  $W_x^{\text{eff}}$  (blue data). The MG is simulated in three dimensions with Floquet periodicity in the y-direction, while the solid-line grating is simulated in two dimensions. Both geometries assume no silicon substrate and an infinite oxide cladding. The two simulations model the same solid-line geometry (Fig. 2(b)), when  $W_y = \Lambda_y$  and thus  $W_x^{\text{eff}} = W_x = 50$  nm, and where  $\theta_0 \approx 2^\circ$  and  $\Gamma_0 \approx 0.014 \mu\text{m}^{-1}$ . Importantly, as  $W_x^{\text{eff}}$  is decreased, the two simulated gratings follow nearly identical trends, indicating an equivalency between the MG and its solid-line counterpart. As a result, two-dimensional simulations of solid-line gratings can be used to approximate the performance of MG designs and calculate grating apodization with fewer computational resources. Quantifying the accuracy of this approximation would be improved with more computational power than used presently. For example, when  $W_x^{\text{eff}}$  is less than 20 nm, the MG decay lengths, obtained by fitting the field intensity, are an order of magnitude longer than the simulation size. Above 20 nm, the two simulations agree to within 15 % for  $\Gamma$  and 3 % for  $\theta$ . Simulating longer gratings would provide a more accurate comparison at small  $W_x^{\text{eff}}$ .

We observe similar trends in Fig. 2(c-d) with experimentally fabricated devices. These devices were fabricated as uniform MGs with nominally the same geometries as described for the MG simulations. MGs with several  $\Lambda_y$  as well as gratings with solid grating lines were fabricated with their decay profiles and outcoupling angles measured. The measured profiles for devices fabricated with  $\Lambda_y = 200$  nm are provided in Fig. S2 in the Supplement 1. The experimental trends follow the simulations very closely. At smaller  $W_x^{\text{eff}}$  the experimentally measured  $\Gamma$  are slightly stronger than simulation, which is likely due to imperfect oxide filling of structures with smaller meta-elements.

### 3. Calculation of grating apodization

The results from Fig. 2 indicate that MG designs are well approximated by gratings with fill-fraction equivalent solid lines, which can be modeled in two dimensions. This approximation enables faster calculation of grating apodization, which we obtain from two finite element simulations. The first simulation performs a gradient descent optimization on a two-dimensional unit cell (inset in Fig. 3(a)) to find the period  $\Lambda_x$  that outcouples light at a design angle of  $\theta = 30^\circ$  for different  $W_x^{\text{eff}}$  and grating line depths. We solve a variant of the inverse problem and find the  $\Lambda_x$  that optimizes the power coupled into the slab mode from free space, assuming the cladding thickness extends indefinitely. The results from this simulation are shown in Fig. 3(a), illustrating that small variations around  $\Lambda_x \approx 200$  nm are required to maintain a uniform phase front along the grating. This is because as the higher index dielectric is removed when the grating element is etched deeper and wider, less phase is accumulated by the slab mode over the unit cell, and  $\Lambda_x$  must be slightly increased to match momentum with the free-space wave. The slight variations in  $\Lambda_x$  can be readily reproduced using electron-beam lithography and modified to adjust beam collimation off chip. The calculated data are fitted to a polynomial regression (black lines), which are used for interpolation of the apodization.

The second simulation models a uniform grating of many lines with period  $\Lambda_x$ , obtained from the first simulation. We calculate  $\Gamma$ , shown in Fig. 3(b), from the obtained decay profile (yellow curve in the inset), as the slab mode enters the grating from one side.  $\Gamma$  depends on the cladding thicknesses, so we simulate our experimental geometry with top and bottom cladding thicknesses of 0.5  $\mu\text{m}$  and of 2.6  $\mu\text{m}$ , respectively. The bottom cladding thickness can be chosen to provide constructive interference for maximal vertical outcoupling of power from the chip. The maximal simulated vertical outcoupling efficiency is  $\approx 56$  % and the minimal is  $\approx 39$  % based on simulations with varied cladding thicknesses. Simulation data are fitted to inverse

polynomial regressions constructed such that  $\Gamma \rightarrow 0$  as  $W_x^{\text{eff}} \rightarrow 0$ . We mark the extrema from Fig. 1(d) along the vertical axis and clearly see that the etch depth must be at least 30 nm (yellow data) to reach the maximum required  $\Gamma$ , which occurs with nearly 50 % duty cycle gratings, i.e., when  $W_x^{\text{eff}} \approx \Lambda_x/2 \approx 100$  nm.

The dynamic range of  $\Gamma$  is largely independent of the grating depth, but it increases rapidly with the inclusion of smaller  $W_x^{\text{eff}}$  grating elements. Solid-line gratings, with  $W_x^{\text{eff}}$  limited to be greater than 30 nm, provide a dynamic range of  $(6.7 \pm 0.2)$  dB, while the MG design, with  $W_x^{\text{eff}}$  limited to be greater than 4.5 nm, increases that range by  $(16.1 \pm 0.1)$  dB for a total range of  $(22.8 \pm 0.3)$  dB. All reported uncertainties are one standard deviation. Here the uncertainties are calculated from the variance in  $\Gamma$  for the different etch depths. The increase in dynamic range enables a smoother onset and improved reproduction of the desired Gaussian beam profile as seen in Fig. 3(c). For simplicity, we consider symmetric truncation, implying that some power will pass un-outcoupled through the grating. We show later how outcoupling can be maximized for a given truncated profile. If we assume that the depth of the grating can be freely chosen to match  $w_0$  then the dynamic range has a one-to-one correspondence with the truncation length (see Fig. S3 in the Supplement 1). A Gaussian profile truncated to  $\approx 1.28 w_0$  can be realized using the MG dynamic range, in contrast with the  $\approx 0.47 w_0$  truncation required by solid-line gratings. This difference is illustrated in the insets of Fig. 3(c). The profiles are better reproduced with the MG design (black profile), with the intensity range of control increasing from  $\approx 35$  % for solid gratings to  $\approx 96$  % for MGs.

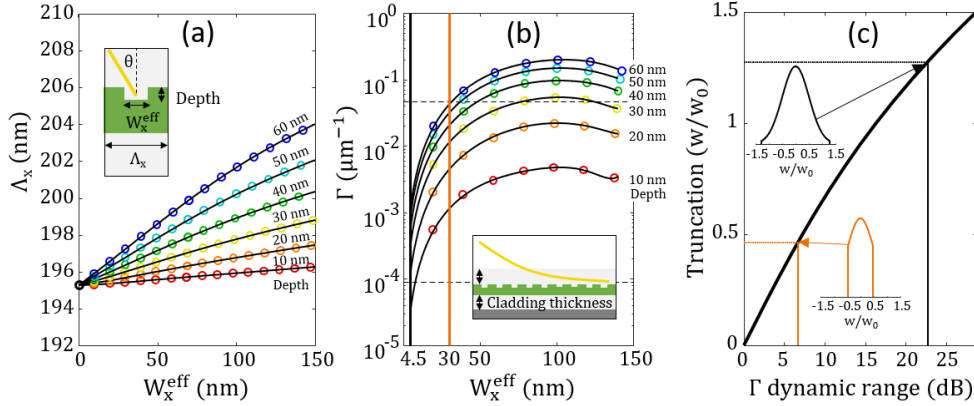


Fig. 3. Parameterization of the grating design. (a) Calculated  $\Lambda_x$  with corresponding polynomial fits (black lines) for gratings that outcouple at  $\theta = 30^\circ$  into free space as a function of different grating depths and effective line widths. The inset shows the simulated unit-cell geometry that has periodic boundary conditions along the x-direction. (b) Calculated  $\Gamma$  with corresponding inverse polynomial fits (black lines) for uniform gratings with varied effective line widths and etch depths. The inset shows the two-dimensional geometry of the simulation, including top and bottom claddings and a silicon substrate. Horizontal dashed lines delineate the dynamic range of  $\Gamma$  from Fig. 1(d) and vertical lines at 30 nm (orange) and 4.5 nm (black) mark the minimum feature sizes for solid-line gratings and MG designs, respectively. (c) Required truncation of the Gaussian beam profile as a function of the  $\Gamma$  dynamic range. The orange and black lines and corresponding insets indicate the truncation for the solid-line grating and MG designs, respectively.

A 30 nm etch depth provides the best coverage for a beam designed with a single etch step and  $w_0 = 100 \mu\text{m}$ . The tradeoffs in apodizing at different etch depths are illustrated in Fig. 4, which plots the beam intensity and phase profiles (panels a-f) and corresponding apodized designs (panels g-l) for different etch depths. The apodized designs are obtained using the results from Fig. 3 by calculating how  $W_x^{\text{eff}}$  and  $\Lambda_x$  must change along the length of the grating to produce the desired beam profile according to eq (1). To calculate the optimal apodization,

we truncate the Gaussian profiles for the given dynamic range of  $\Gamma$  to produce symmetric beam profiles.

While ideal beam profiles have a smooth onset,  $\Gamma$  cannot be made arbitrarily weak since the minimum  $W_x^{\text{eff}}$  is fixed to 4.5 nm. The weakest  $\Gamma$  for each etch depth sets how steep the beam profile will be at its onset. Deeper etched gratings cause more abrupt onsets as seen in Fig. 4(e-f). There is a different tradeoff for shallower etched gratings—that less total power will be outcoupled from the slab mode over the same grating length. Weaker outcoupling allows some power to continue past the grating region. For example, the MGs with 10 nm and 20 nm etch depths only outcouple  $\approx 42\%$  and  $\approx 95\%$  of the available slab-mode power, respectively, while gratings with 30 nm or deeper etch depths can outcouple more than 99% of the power. These percentages correspond to the amount of power leaving the slab mode, the efficiency of outcoupling vertically up versus down will depend on the exact cladding thickness and design of the grating substrate. Despite having truncated profiles, the deeper etched gratings can outcouple all the power by continuing the grating beyond where the beam is truncated. This leads to the exponential tails seen in Figs. 4(c-f) corresponding to the flat apodization in Figs. 4(i-l). While the beam profile is more accurately reproduced at the shallower etch depths, there is not enough grating length to outcouple all the power from the slab mode. As a result, the outcoupling strength is modulated with a shape similar to the beam profile itself, as seen in Fig. 4(g) compared to Fig. 4(a). In contrast, the design with the optimal etch depth around 30 nm has a nearly linear apodization (Fig. 4(i)). In all cases, the simulated apodizations produce beams with nearly flat phase profiles indicating that the calculated apodization follows well from the simulations in Fig. 3 and that the resulting beams should be nearly collimated.

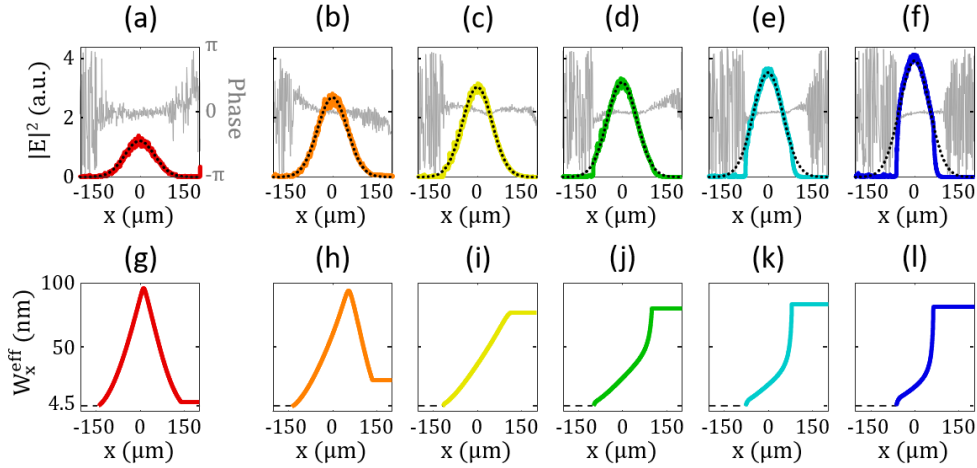


Fig. 4. Effect of etch depth on beam performance (a-f) Beam profiles (colored red to blue) and phase profiles (gray) obtained by two-dimensional simulation of solid-line gratings with apodizations calculated for different etch depths ranging from 10 nm to 60 nm, according to the colors introduced in Fig. 3. The y-axes are shared amongst panels a-f. (g-l) the apodization profiles used to generate the gratings simulated in (a-f). Each design begins with  $W_x^{\text{eff}} = 4.5$  nm and is apodized according to a truncated Gaussian beam profile with a waist of 100  $\mu\text{m}$  such that the outcoupled beam is symmetric. The y-axes are shared amongst panels g-l.

#### 4. Experimental meta-grating results

To maximize power outcoupling we choose an etch depth of nominally 37 nm for calculating our apodized design. We require two beam designs, one emitting nominally around  $30^\circ$  and the other around  $8^\circ$ . Both designs incorporate the same EVC, producing a nominal slab-mode beam waist of 100  $\mu\text{m}$ . In the second stage, two different MGs are designed, producing numerically-

simulated beam waists of  $\approx 134 \mu\text{m}$  and  $\approx 71 \mu\text{m}$  for the  $\approx 30^\circ$  and  $\approx 8^\circ$  beams respectively. Both gratings were designed using  $\Lambda_y = 120 \text{ nm}$ . The previous analysis is then carried out according to eq (1) using these different beam waists for their corresponding outcoupling angles.

To fabricate our devices we use stoichiometric  $\text{Si}_3\text{N}_4$  and two separate electron-beam lithography and reactive-ion etch steps. We use a through etch to fabricate the EVC and a nominal  $37 \text{ nm}$  partial etch to fabricate the MG. The device has a thermal oxide bottom cladding with a nominal thickness of  $2.6 \mu\text{m}$  and is overgrown with a top oxide cladding using a low temperature oxide LPCVD process. The details of the fabrication process as well as SEM images of devices are provided in Fig. S4 and Fig. S5, respectively, in the Supplement 1. After depositing the cladding, the wafers are diced and the edges of the chip are then polished to expose waveguides terminated with a tapered edge coupler [25], which is used for coupling laser light on-chip with a cleaved fiber. Our measurement setup uses a  $20\times 0.75 \text{ NA}$  objective mounted to a micrometer stage for imaging the grating emission onto a CCD camera and measuring the beam profile at different heights above the chip surface.

Fig. 5(a) shows an optical image of the beam emitted from the fabricated device of the  $30^\circ$  design. The blue arrow indicates the direction of the slab mode beam (not visible) coming from the EVC. Fig. 5(b) and (c) show the beam profile along the x and y-directions (with power integrated over the orthogonal direction) along with Gaussian fits. The beam has a fitted waist along x and y of  $w_x = (128 \pm 0.5) \mu\text{m}$  and  $w_y = (81 \pm 0.2) \mu\text{m}$ , respectively, where the uncertainty is obtained from Gaussian fitting parameter variance estimate. By measuring the beam at different heights off the chip (Fig. 5(d)) we obtain a measured value of  $\theta = 30.1^\circ \pm 0.1^\circ$ , where the uncertainty is obtained from fitting the beam trajectory to a straight line. As the beam propagates, the profile slightly focuses along the x and y directions as shown in Figs. 5(d, e). The focusing along x corresponds to an accumulation of phase along the length of the grating equivalent to approximately one  $\lambda$  over a length of  $800 \lambda$ , which can be corrected by slightly modifying the results from the period simulation in Fig. 3(a). Figs. 5(f-j) show the corresponding measurements for the fabricated  $8^\circ$  device, which give  $w_x = (89 \pm 0.7) \mu\text{m}$  and  $w_y = (80 \pm 0.2) \mu\text{m}$ ,  $\theta = 8.69^\circ \pm 0.02^\circ$ , and a focusing along the x direction equivalent to an excess accumulation of  $\lambda$  phase over a length of  $\approx 725 \lambda$ . The performance of the EVC is functionally equivalent between the two devices, with  $w_y \approx 80 \mu\text{m}$  at  $z = 0 \text{ mm}$  and a similar  $w_y$  trend at different heights (Figs. 5(e) and (j)), but the  $30^\circ$  MG device matches the design parameters better than the  $8^\circ$  device. By incorporating feedback from experimentation to our apodization design, modifications can be made to further improve beam performance. Higher resolution images of the beam profiles at different heights shown in Figs. 5(d) and 5(i) are provided in Fig. S6 in the Supplement 1. While similarly good phase and angular performance can be achieved without utilizing a subwavelength MG design, it would have been impossible to successfully reproduce Gaussian beam profiles along the x-direction using solid grating lines. Attempts to do so yield beam profiles that were exponentially decaying, as seen in Fig. S7 in the Supplement 1.

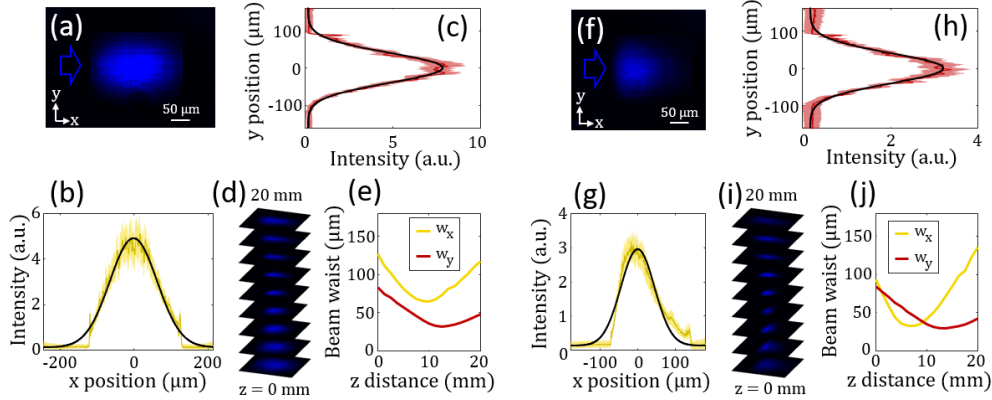


Fig. 5. Experimental results. (a) Optical image of the beam designed to emit at  $\approx 30^\circ$  from the MG. The slab mode beam is incident along the x direction from the left (denoted with a blue arrow). (b) Intensity profile of the beam along the length of the grating with a Gaussian fit (black line). The light yellow region corresponds to a one standard deviation measurement uncertainty of the beam intensity profile, obtained from different horizontal slices of the profile from panel a, while the dark yellow corresponds to the mean profile. (c) Intensity profile of the beam orthogonal to the grating with a Gaussian Fit (black line). The light red region corresponds to a one standard deviation measurement uncertainty of the beam intensity profile, obtained from different vertical slices of the profile from panel a, while the dark red corresponds to the mean profile. (d) Optical images of the beam taken at different heights above the chip. The separation between images is 2.5 mm. (e) Measured beam waist along x and y directions, yellow and red respectively, as a function of distance from the chip surface. (f-j) Data like that shown in panels (a-e), but for a beam designed with a narrower beam waist along the x direction that emits at  $\approx 8^\circ$  from the MG.

## 5. Conclusions

In this paper, we presented the experimental realization of grating outcouplers based on a subwavelength MG design that produces pristine beam profiles at blue visible wavelengths. We established the equivalency between MG designs and designs using solid grating lines, which enabled a speed up in the modeling of our fabricated structures by reducing the simulations from three to two dimensions. Through our two-dimensional analysis we explained the tradeoffs between choosing different etch depths for creating apodized gratings with large beam waists. Our design protocol is robust for calculating the apodizations of different beam shapes and beam angles and allowed us to push the limits of how large a beam can be designed at short wavelengths within the resolution of electron beam lithography. We showed that by using a MG design we could improve the dynamic range of the outcoupling strength by  $\approx 16$  dB and increase the range of control over the intensity profile by  $\approx 60\%$  compared to solid-line gratings. At 461 nm this improvement effectively differentiates between being able to accurately reproduce Gaussian beams and not.

The developed techniques and demonstrated devices extend the capabilities of on-chip photonic technologies, particularly for miniaturizing devices for quantum metrology and sensing. In the future, we plan to incorporate beams at different angles and with different colors on the same chip and integrate with meta-surfaces for controlling beam phase fronts and polarizations within a fully-planar structure. These devices will enable new on-chip technologies for interrogating atoms and other quantum media within small working volumes. By maintaining precise control of the beam properties, future designs may be able to incorporate anisotropic meta-grating elements to create beams with non-traditional polarizations and angular momenta for customizable design of integrated quantum devices.

## Acknowledgements

The research was partially funded by the U.S. Defense Advanced Research Projects Agency (DARPA) under the Atomic-Photonic (A-PhI) program. The views and conclusions are those of the authors and should not be interpreted as representing the official policies of the funding agency. Dr. Chad Ropp and Dr. Alex Yulaev also acknowledge support under the Professional Research Experience Program (PREP), administered through the Department of Chemistry and Biochemistry, University of Maryland. Research performed in part at the National Institute of Standards and Technology Center for Nanoscale Science and Technology. We also would like to thank William McGehee, Kartik Srinivasan, and Jinghui Yang for helpful discussions.

## Disclosures

The authors declare no conflicts of interest.

## Data availability

Data underlying the results presented in this paper may be obtained from the authors upon reasonable request.

## Supplemental document

See Supplement 1 for supporting content.

## References

1. V. M. N. Passaro, C. D. Tullio, B. Troia, M. L. Notte, G. Giannoccaro, and F. D. Leonardis, "Recent Advances in Integrated Photonic Sensors," *Sensors* **12**, 15558–15598 (2012).
2. J. Kitching, E. A. Donley, S. Knappe, M. Hummon, A. T. Dellis, J. Sherman, K. Srinivasan, V. A. Aksyuk, Q. Li, D. Westly, B. Roxworthy, and A. Lal, "NIST on a Chip: Realizing SI units with microfabricated alkali vapour cells," *J. Phys.: Conf. Ser.* **723**, 012056 (2016).
3. J. Wang, F. Sciarrino, A. Laing, and M. G. Thompson, "Integrated photonic quantum technologies," *Nature Photonics* **14**, 273–284 (2020).
4. M. T. Hummon, S. Kang, D. G. Bopp, Q. Li, D. A. Westly, S. Kim, C. Fredrick, S. A. Diddams, K. Srinivasan, V. Aksyuk, and J. E. Kitching, "Photonic chip for laser stabilization to an atomic vapor with  $10^{-11}$  instability," *Optica*, *OPTICA* **5**, 443–449 (2018).
5. K. K. Mehta, C. Zhang, M. Malinowski, T.-L. Nguyen, M. Stadler, and J. P. Home, "Integrated optical multi-quantum logic," *Nature* **586**, 533–537 (2020).
6. K. K. Mehta, C. D. Bruzewicz, R. McConnell, R. J. Ram, J. M. Sage, and J. Chiaverini, "Integrated optical addressing of an ion qubit," *Nature Nanotechnology* **11**, 1066–1070 (2016).
7. R. J. Niffenegger, J. Stuart, C. Sorace-Agaskar, D. Kharas, S. Bramhavar, C. D. Bruzewicz, W. Loh, R. T. Maxson, R. McConnell, D. Reens, G. N. West, J. M. Sage, and J. Chiaverini, "Integrated multi-wavelength control of an ion qubit," *Nature* **586**, 538–542 (2020).
8. Y. R. P. Sortais, H. Marion, C. Tuchendler, A. M. Lance, M. Lamare, P. Fournet, C. Armellin, R. Mercier, G. Messin, A. Browaeys, and P. Grangier, "Diffraction-limited optics for single-atom manipulation," *Phys. Rev. A* **75**, 013406 (2007).
9. G. W. Hoth, E. A. Donley, and J. Kitching, "Atom number in magneto-optic traps with millimeter scale laser beams," *Opt. Lett.*, *OL* **38**, 661–663 (2013).
10. N. Chauhan, D. Bose, M. Puckett, R. Moreira, K. Nelson, and D. J. Blumenthal, "Photonic Integrated Si<sub>3</sub>N<sub>4</sub> Ultra-Large-Area Grating Waveguide MOT Interface for 3D Atomic Clock Laser Cooling," in *2019 Conference on Lasers and Electro-Optics (CLEO)* (2019), pp. 1–2.
11. A. Yulaev, W. Zhu, C. Zhang, D. A. Westly, H. J. Lezec, A. Agrawal, and V. Aksyuk, "Metasurface-Integrated Photonic Platform for Versatile Free-Space Beam Projection with Polarization Control," *ACS Photonics* **6**, 2902–2909 (2019).
12. A. Yariv and P. Yeh, *Photonics: Optical Electronics in Modern Communications*, 6th edition (Oxford University, 2006).
13. R. Halir, P. Cheben, S. Janz, D.-X. Xu, Í. Molina-Fernández, and J. G. Wangüemert-Pérez, "Waveguide grating coupler with subwavelength microstructures," *Opt. Lett.*, *OL* **34**, 1408–1410 (2009).

14. X. Chen, K. Xu, Z. Cheng, C. K. Y. Fung, and H. K. Tsang, "Wideband subwavelength gratings for coupling between silicon-on-insulator waveguides and optical fibers," *Opt. Lett.*, **OL 37**, 3483–3485 (2012).
15. X. Xu, H. Subbaraman, J. Covey, D. Kwong, A. Hosseini, and R. T. Chen, "Complementary metal–oxide–semiconductor compatible high efficiency subwavelength grating couplers for silicon integrated photonics," *Appl. Phys. Lett.* **101**, 031109 (2012).
16. Z. Cheng, X. Chen, C. Y. Wong, K. Xu, and H. K. Tsang, "Apodized focusing subwavelength grating couplers for suspended membrane waveguides," *Appl. Phys. Lett.* **101**, 101104 (2012).
17. R. Halir, P. J. Bock, P. Cheben, A. Ortega-Moñux, C. Alonso-Ramos, J. H. Schmid, J. Lapointe, D.-X. Xu, J. G. Wangüemert-Pérez, Í. Molina-Fernández, and S. Janz, "Waveguide sub-wavelength structures: a review of principles and applications," *Laser & Photonics Reviews* **9**, 25–49 (2015).
18. J. H. Song, T. D. Kongnyuy, B. Troia, S. S. Saseendran, P. Soussan, R. Jansen, and X. Rottenberg, "Grating devices on a silicon nitride technology platform for visible light applications," *OSA Continuum, OSAC* **2**, 1155–1165 (2019).
19. D. J. Blumenthal, "Photonic integration for UV to IR applications," *APL Photonics* **5**, 020903 (2020).
20. F. Sorrentino, G. Ferrari, N. Poli, R. Drullinger, and G. M. Tino, "Laser cooling and trapping of atomic strontium for ultracold atoms physics, high-precision spectroscopy and quantum sensors," *Mod. Phys. Lett. B* **20**, 1287–1320 (2006).
21. T. L. Nicholson, S. L. Campbell, R. B. Hutson, G. E. Marti, B. J. Bloom, R. L. McNally, W. Zhang, M. D. Barrett, M. S. Safronova, G. F. Strouse, W. L. Tew, and J. Ye, "Systematic evaluation of an atomic clock at  $2 \times 10^{-18}$  total uncertainty," *Nature Communications* **6**, 6896 (2015).
22. J. M. Luque-González, A. Herrero-Bermello, A. Ortega-Moñux, Í. Molina-Fernández, A. V. Velasco, P. Cheben, J. H. Schmid, S. Wang, and R. Halir, "Tilted subwavelength gratings: controlling anisotropy in metamaterial nanophotonic waveguides," *Opt. Lett.*, **OL 43**, 4691–4694 (2018).
23. S. Kim, D. A. Westly, B. J. Roxworthy, Q. Li, A. Yulaev, K. Srinivasan, and V. A. Aksyuk, "Photonic waveguide to free-space Gaussian beam extreme mode converter," *Light: Science & Applications* **7**, 72 (2018).
24. D. Taillaert, P. Bienstman, and R. Baets, "Compact efficient broadband grating coupler for silicon-on-insulator waveguides," *Opt. Lett.*, **OL 29**, 2749–2751 (2004).
25. R. Marchetti, C. Lacava, L. Carroll, K. Gradkowski, and P. Minzioni, "Coupling strategies for silicon photonics integrated chips [Invited]," *Photon. Res.*, **PRJ 7**, 201–239 (2019).

## Supplementary Information

### Meta-grating outcouplers for optimized beam shaping in the visible

**CHAD ROPP,<sup>1,2</sup> ALEXANDER YULAEV,<sup>1,2</sup> DARON WESTLY,<sup>1</sup> GREGORY SIMELGOR,<sup>1</sup> AND VLADIMIR AKSYUK<sup>1</sup>**

*<sup>1</sup>Physical Measurement Laboratory, National Institute of Standards and Technology, Gaithersburg, Maryland 20899, USA*

*<sup>2</sup>Department of Chemistry and Biochemistry, University of Maryland, College Park, MD 20742, USA*

Included data: 7 Supplementary figures.

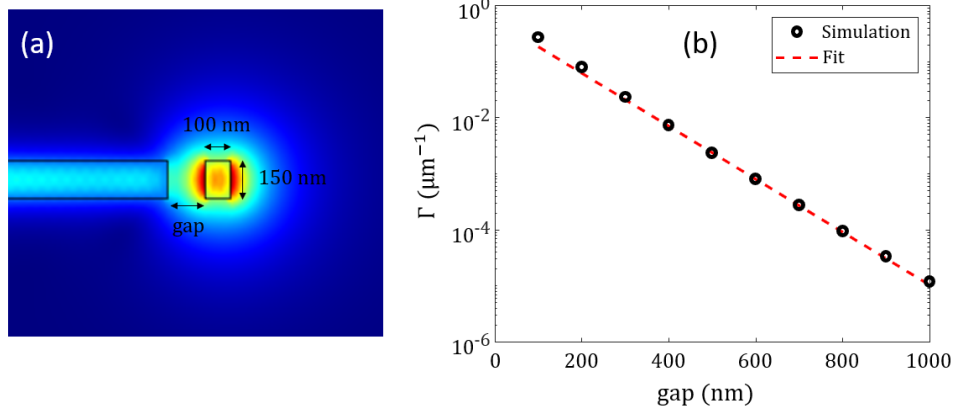


Fig. S1. (a) Simulated cross section of the evanescent coupler (EVC) with the slab mode on the left and the waveguide on the right. The transverse electric field mode is shown evanescently coupling from the waveguide into the slab mode. (b) Coupling strength calculated as a function of the gap between the waveguide and the dielectric slab. Many orders of magnitude in coupling strength can be achieved by varying the gap separation.

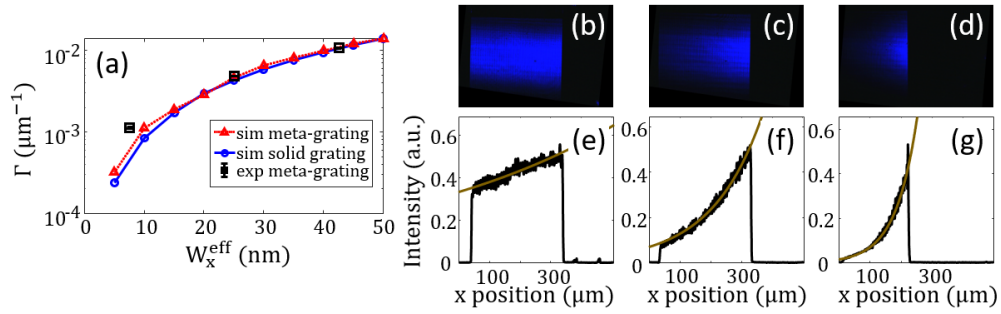


Fig. S2. (a) The calculated outcoupling strength of the simulated meta-grating (MG) (red), simulated solid-line grating (blue), and experimentally fabricated MGs with  $\Lambda_y = 200$  nm (black data) as a function of  $W_x^{\text{eff}}$ . This panel is taken from Fig. 2(c) in the main text. (b-c) Experimentally measured optical images of the beams emitted from the uniform MG with  $W_x^{\text{eff}} = \{7.5, 25, 42.5\}$ , respectively. (e-g) Projections of the beam profiles along the x direction for the images shown in panels (b-d), respectively. Each profile is fitted to an exponential decay to extract  $\Gamma$ , which is the inverse of the fitted decay length. The error bars in panel a correspond to one standard deviation statistical uncertainty of these fits.

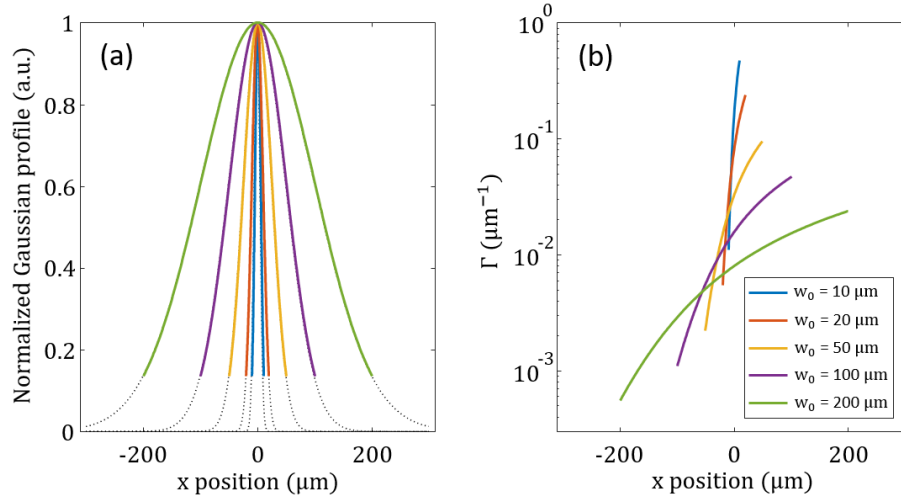


Fig. S3. (a) Gaussian profiles with varying waists,  $w_0$  (colors corresponding to legend in panel b), all truncated at  $1/w_0$ . (b) The calculated outcoupling strength as a function of position required to reproduce each of the profiles in panel a. Narrower waists require stronger outcoupling strengths, however, the outcoupling range remains the same, equal to 16.33 dB, for all Gaussian profile with the same truncation.

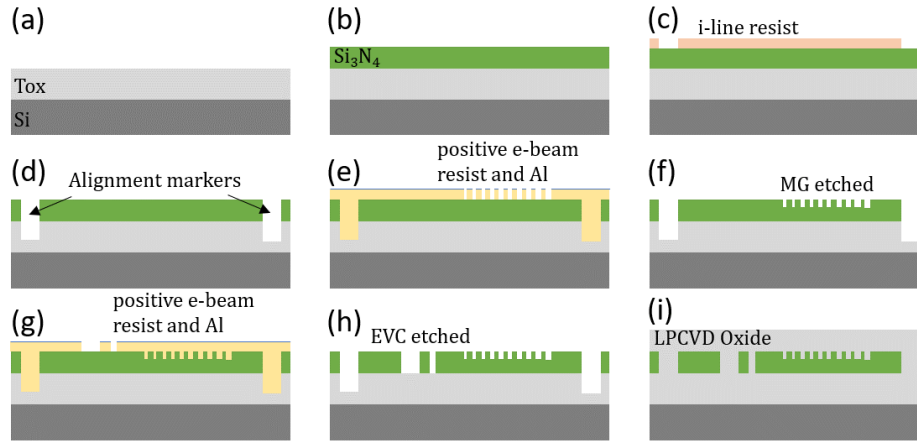


Fig. S4. Fabrication process. (a) To fabricate our devices we start with bare, single side polished silicon wafers and grow nominally  $2.6 \mu\text{m}$  of thermal oxide using a wet oxidation process at  $1150^\circ\text{C}$ . The oxide is measured using a spectroscopic ellipsometer and can be controllably thinned to the correct desired thickness using a solution 6:1 buffered hydrofluoric acid. (b) We then deposit stoichiometric  $\text{Si}_3\text{N}_4$  on these wafers using low-pressure chemical vapor deposition (LPCVD) with the following conditions: temperature =  $775^\circ\text{C}$ , pressure =  $300 \text{ Pa}$ , and a 15:1 gas ratio of  $\text{NH}_3$  to dichlorosilane. (c) The wafers are coated with an optical resist and two sets of alignment marks are patterned using an i-line optical stepper. (d) After development, these alignment marks are etched  $500 \text{ nm}$  deep using a  $150 \text{ W}$ ,  $\text{CF}_4$  plasma in a parallel plate etcher then cleaned for  $20 \text{ min}$  in 3:1 solution of sulfuric acid/hydrogen peroxide (piranha) and rinsed in deionized water. (e) They are then coated with  $100 \text{ nm}$  of a positive tone e-beam resist. A  $15 \text{ nm}$  aluminum layer is deposited using thermal evaporation to act as a conductive layer during the electron beam exposure. The MGs are then patterned using one set of the previously defined alignment marks. After exposure, the wafers are developed for  $75 \text{ s}$  in hexyl acetate at  $4^\circ\text{C}$  and rinsed with isopropyl alcohol (IPA). (f) The MGs are then etched in a  $150 \text{ W}$ ,  $\text{CHF}_3/\text{O}_2$  plasma to the required depth. (g) The wafers are then cleaned, coated with  $350 \text{ nm}$  of the positive e-beam resist and  $15 \text{ nm}$  of aluminum, and the EVCs, waveguides, and tapered edge couplers are exposed using the second set of previously defined alignment marks. The wafers are developed for  $75 \text{ s}$  in hexyl acetate at  $4^\circ\text{C}$  and rinsed with IPA. (h) The wafers are then etched in a  $150 \text{ W}$ ,  $\text{CHF}_3/\text{O}_2$  plasma. (i) After cleaning, a top cladding is added using a low temperature oxide LPCVD process.

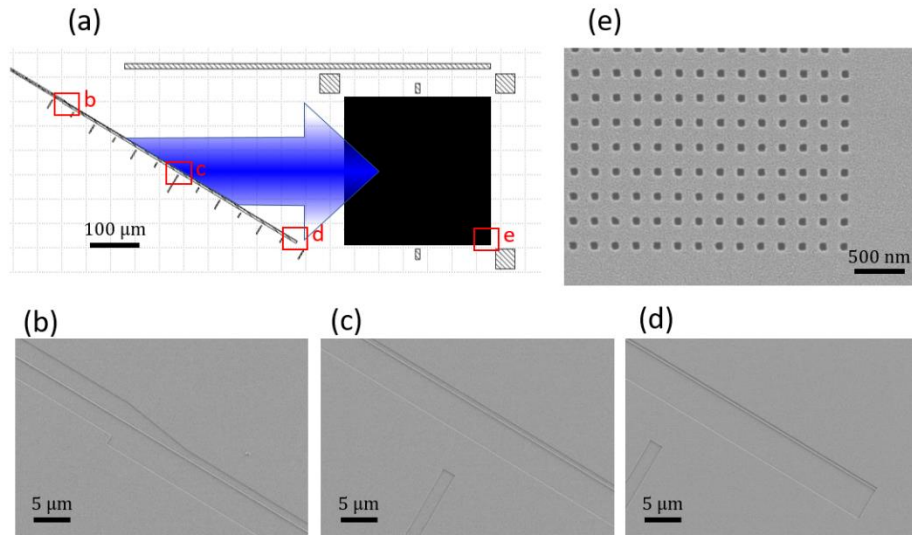


Fig. S5. (a) Diagram of a test extreme mode converter device consisting of an EVC on the left and a MG outcoupler on the right. The blue arrow indicates the path of the slab mode beam produced by the EVC propagating toward the MG. (b) SEM image of the beginning of the EVC where the waveguide is transitioned to be closer to the dielectric slab and whose location is indicated in red in panel a. (c) SEM image of the middle of the EVC whose location is indicated in red in panel a. (d) SEM image of the end of the EVC whose location is indicated in red in panel a. Power is transferred to the slab mode as the waveguide is brought closer to the dielectric slab. By the end of the EVC minimal power remains in the waveguide. (e) SEM image of the MG whose location is indicated in red in panel a. In this test device the MG elements have been etched all the way through the nitride layer and the grating periods are  $\Lambda_y = 250$  nm and  $\Lambda_x = 216$  nm with the square MG elements nominally defined to be 64 nm in size at this location in the grating structure.

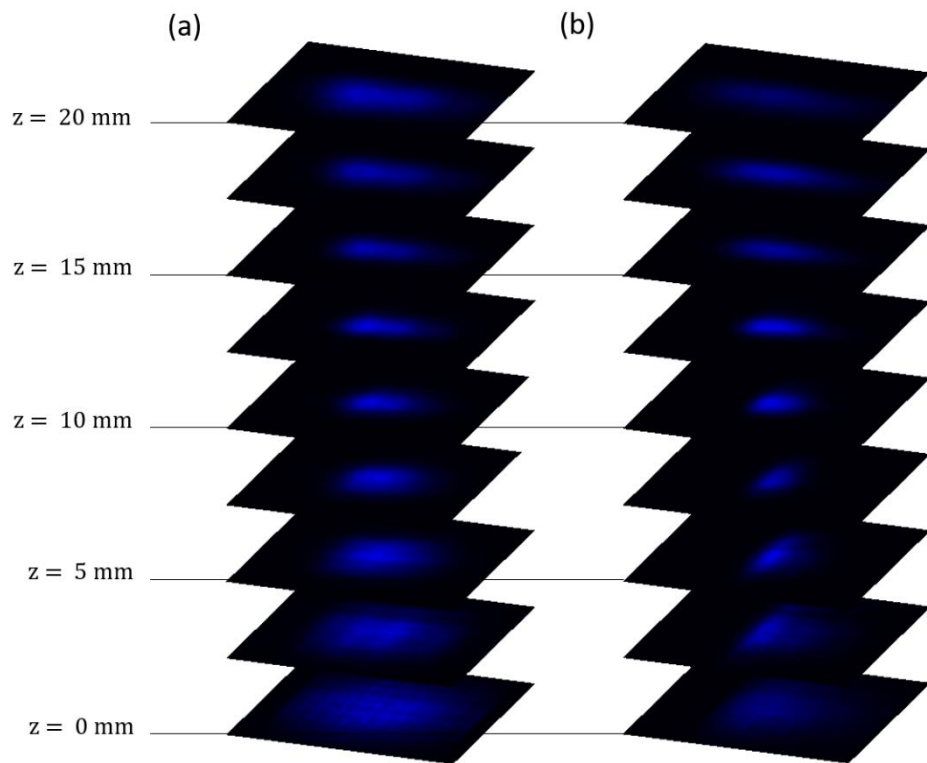


Fig. S6. (a) Optical images of the  $30^\circ$  beam taken at different  $z$ -heights above the chip. (b) Optical images of the  $8^\circ$  beam taken at different  $z$ -heights above the chip. These panels are higher resolution versions of Figs. 5(d) and 5(i) in the main text.

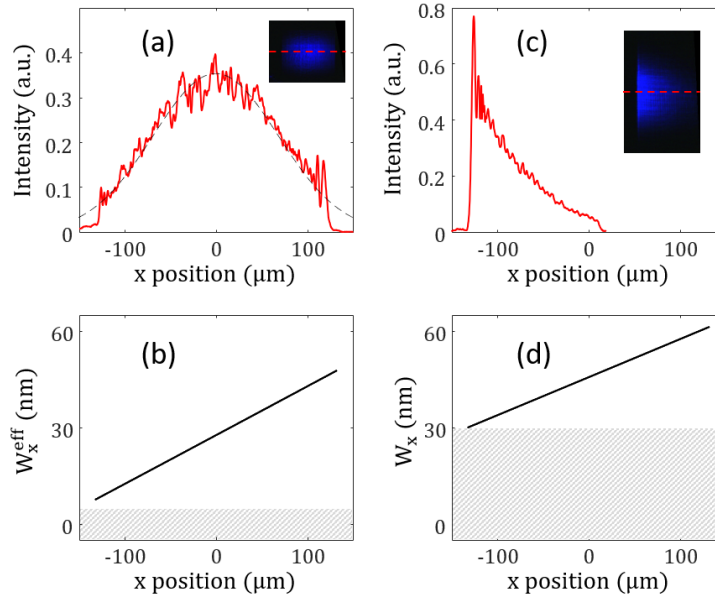


Fig. S7. Experimental comparison of a MG beam with a solid-line grating beam. (a) Cross sectional profile of the beam produced by a MG along with a Gaussian fit (black line). The inset shows an image of the measured beam. (b) Plot of the  $W_x^{\text{eff}}$  apodization for the MG showing a minimum chosen  $W_x^{\text{eff}} = 7.5$  nm. With a MG approach the minimum effective feature size can be as small as 4.5 nm (gray region) (c) Cross sectional profile of the beam produced by a solid-line grating, which follows an exponential-like decay profile. The inset shows an image of the measured beam. (d) Plot of the  $W_x$  apodization for the solid-line grating showing a minimum  $W_x = 30$  nm limited by the fabrication process (gray region). Both gratings produce beams with an outcoupling angle of  $\approx 30^\circ$ .